

JGR Earth Surface

RESEARCH ARTICLE

10.1029/2019JF005500

Key Points:

- Block collision on soft surfaces is modelled and dissipation parameters are identified for concrete blocks on sandy substrate
- Image processing is performed to reconstruct the bloc trajectories
- Rebonds are characterized from a stochastic viewpoint

Correspondence to:

V. Richefeu,
vincent.richefeu@3sr-grenoble.fr

Citation:

Garcia, B., Richefeu, V., Baroth, J., Daudon, D., & Villard, P. (2020). Collision of shaped boulders with sand substrate investigated by experimental, stochastic, and discrete approaches. *Journal of Geophysical Research: Earth Surface*, 125, e2019JF005500. <https://doi.org/10.1029/2019JF005500>

Received 6 JAN 2020

Accepted 26 AUG 2020

Collision of Shaped Boulders With Sand Substrate Investigated by Experimental, Stochastic, and Discrete Approaches

B. Garcia^{1,2} , V. Richefeu¹ , J. Baroth¹, D. Daudon¹, and P. Villard¹

¹Univ. Grenoble Alpes, CNRS, Grenoble INP, 3SR, Grenoble, France, ²IMSRN-GINGER, Ingénierie des Mouvements de Sol et Risques Naturels, Montbonnot, France

Abstract This paper focuses on experimental and numerical studies aiming to better characterize the rebound kinematics between a natural soil and rock boulders using single-block collision models. The variability of the dissipative parameters needed to reproduce the experimental results was studied considering two different approaches: stochastic transfer matrix and discrete element model (DEM). An experimental process taking into account all possible variables related to the collision was setup for small-scale tests involving cylindrical and triangular boulders that introduces natural variability during impact. The objective of the experimental tests is to identify the relationship between incident and reflected velocities (before and after impact, respectively), in order to improve the predictability of the two numerical proposed approaches. The experimental results help to quantify the amount of energy losses during impacts and thus expands the knowledge to reproduce more realistic rockfall events. This work is divided in three main axes: (i) statistical analysis of experimental trajectories based on experimental tests; (ii) stochastic approach predicting in a simple way from initial velocities the kinematic of blocks after rebounds; and (iii) calibration of a discrete element model including probabilistic analysis based on Monte Carlo approach. This way, the two collision approaches presented in this work are able to predict rebounds in terms of averages, standard deviations, and distributions.

1. Introduction

In order to improve rockfall modeling, various researchers or scholars, for example, Wu (1985), Hungr and Evans (1988), and Piteau and Clayton (1977), have carried out experimental tests aiming to identify the parameters that better reproduce rebound kinematics. It aims to characterize rather what happens on “soft” substrates (which involve more complex means of dissipation) since they are much more common in the field than hard ground surfaces, such as road embankments, gravel, exposed rock mass, and bedrock.

A number of studies treat this problem based on real scale experimental tests or scaled models. In particular, Chau et al. (2002) conducted an experimental study of block releases using spherical particles impacting a flat and hard surface. The blocks were released vertically, while the impact surface was randomly tilted to assess slope inclination effects on rebound. Dorren et al. (2006) conducted a large-scale test campaign to study the forest effect on block trajectory changes. In this work, lateral spread of the blocks following impacts with trees was assessed from several successive impact points based on the visible traces observed on the ground or tree stems. It is a relatively simple and accurate technique for measuring block deflection; however, it cannot be easily implemented on rocky slopes because bedrock impacts leave less obvious traces.

In general, these experimental data are used to better understand granular flow propagation and interaction (Asteriou & Tsiambaos, 2016; Bourrier et al., 2008, 2012; Labiouse & Heidenreich, 2009; Manzella & Labiouse, 2008; Okura et al., 2000). They are sources of useful information needed to validate different numerical models (Manzella et al., 2011; Mollon et al., 2012), which proved to be able to adequately describe the global behavior (mass flow) of a set of interacting particles or isolated ones. However, experience shows that dissipation phenomena observed in the field remain more complex than in laboratory tests and that further investigative resources are needed to better explore this subject.

Numerical modeling can also be used to perform sensitivity analysis in order to quantify the influence of a single parameter at a time, while the others have a fixed value (normally set to the mean value). Among other

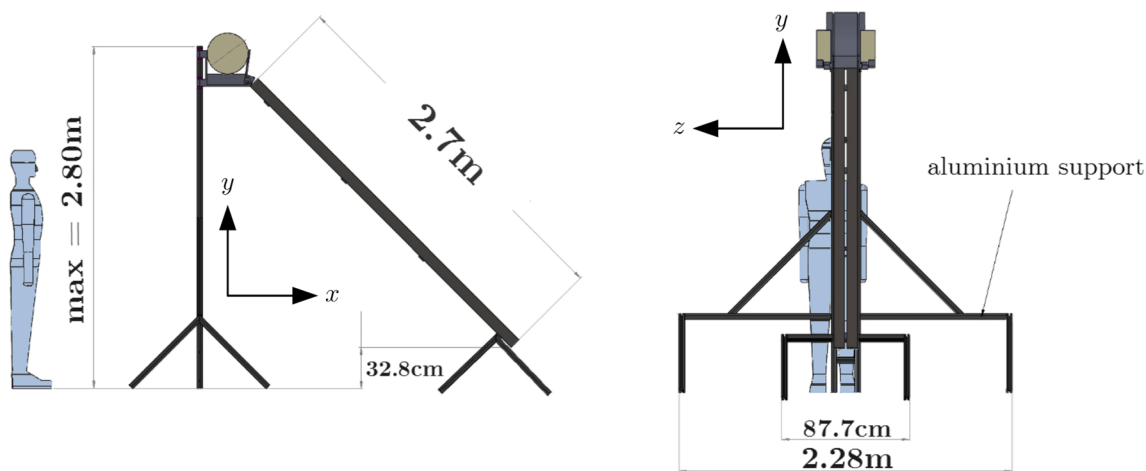


Figure 1. Design of the metal ramp.

approaches, the discrete element method (DEM), as initiated by Cundall and Strack (1979), is a suitable tool for dealing with rockfall phenomena by having some control over the possibility of dissipation at the contact or collision level. This involves simulating the mechanisms of energy dissipation by friction and collision during the propagation of an isolated block on a propagation path or a mass of granular material on a slope (Mollon et al., 2012). The DEM model used in this work explicitly takes into account the shape of the blocks, and special emphasis is placed on the monitoring of the means of dissipating energy by collision, friction, and rolling resistance.

The propagation paths and run-out estimation are subjected to major uncertainties (such as numerical discretization of the slope, soil heterogeneity, and simplicity of the collision model). In this way, taking into account a stochastic model to reproduce collision laws seems suitable and would make possible to incorporate uncertainties in the prediction of rebounds while having some control of their variability. This is the hypothesis adopted by some authors (Bourrier & Hungr, 2011; Dorren & Seijmonsbergen, 2003) for whom bounce kinematics is intrinsically based on a better understanding of parameter variability and uncertainty inherent to the measurements obtained on the field experiments. In these models, the velocities after rebound (reflected velocities) $\mathbf{V}_{\text{out}} = (V_{\text{out}}^x, V_{\text{out}}^y, \omega_{\text{out}})^T$ are related to the incidental rebound velocities $\mathbf{V}_{\text{in}} = (V_{\text{in}}^x, V_{\text{in}}^y, \omega_{\text{in}})^T$ by the following linear relationship :

$$\mathbf{V}_{\text{out}} = \mathbf{A} \cdot \mathbf{V}_{\text{in}} \quad (1)$$

where \mathbf{A} is a 3×3 matrix whose components are referred to as *kinematic restitution coefficients*. However, it is important to note that these coefficients are defined at the scale of singularities in a trajectory and not at the scale of a contact zone between the block and the ground such as the model proposed in this work. Based on the collision model of Equation 1 (nonregular kinematics), Bourrier et al. (2009) proposed in their stochastic model (RockyFOR3D, Dorren, 2016) that the components of the matrix \mathbf{A} may vary according to Gaussian distributions, taking into account for collision hazards and uncertainties. The model developed and used in this manuscript is different from stochastic trajectory models in several aspects, but the experimental data presented here may also help to verify the scope of this approach.

This work deals with the modeling of isolated blocks that propagate on a slope; the blocks and the slope have complex geometries. Three original steps are presented:

1. Experimental approach: an experimental device consisting on a small-scale inclined ramp on which high-performance concrete blocks can roll without slipping and then impact a wooden box filled with natural substrate. A high-speed camera was used to estimate collision velocities in translation and rotation, before and after impact.
2. Stochastic analysis: from the experimental cumulative distributions representing prebounce and postbounce velocities, we proposed and validated a simple trajectory collision model based on the definition of a *stochastic matrix of velocity transfers*. The variability for each identified rebound parameters was assessed.

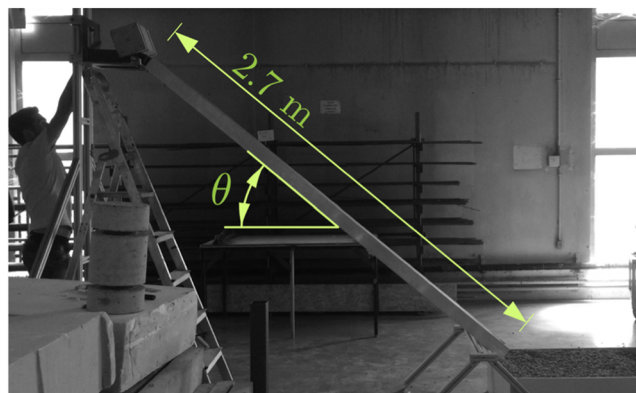


Figure 2. Overview of the experimental setup during a test. Ramp inclination θ can vary between 30° and 60° .

3. Discrete element modeling: experimental results were used to identify DEM contact parameters. For this purpose, reflected experimental velocities V_{out} were compared with velocities calculated under the same impact conditions using DEM numerical model. The relevance of this numerical model was tested by applying a mechanical-probabilistic analysis involving Monte Carlo simulations. Finally, a sensitivity analysis (Sobol indexes) was performed, in order to better understand the influence of DEM collision parameters upon expected output values.

2. Experimental Tests

This section presents (1) experimental device and analysis process used to determine the kinematics of a concrete boulder impacting a sandy substrate; (2) image processing used to define the incident and reflected velocities in each recording; and (3) quantifying different sources of errors.

2.1. Experimental Device

The device, shown in Figure 1, consists of an inclined metal rail, on which a block having two suitable grooves can roll and/or slide along the corners. The rails can be covered with a rough coating to promote nonslip rolling movement. At the end of the ramp, the block performs a short free flight and then collides with granular substrate laid out within a wooden box and then bounces. The rail, measuring 2.7 m long, has an adjustable inclination that may vary from 30° to 60° (Figure 2). Once set to its highest position, the ramp can reach a maximum high of 2.8 m, whence blocks are released. For this experimental campaign, the inclination of the ramp was set to 45° (Garcia et al., 2017). The wooden box in which the collision occurs (rectangular box; 1 m length, 0.7 m width, and 0.25 m height) can be filled up with any type of substrate. For this study, it was filled with fine dry sand. At the end of each test, in order to prepare for the next release, impacted surface is straightened up using a cleat.



Figure 3. A digital camera is positioned at the bottom of the ramp to capture the kinematics of the block during its impact with the ground, producing the better quality frames used for trajectory reconstruction. The camera is positioned far enough from the impact point to limit (1) the “wide angle” lens distortion and (2) vibration effects that may affect image quality.

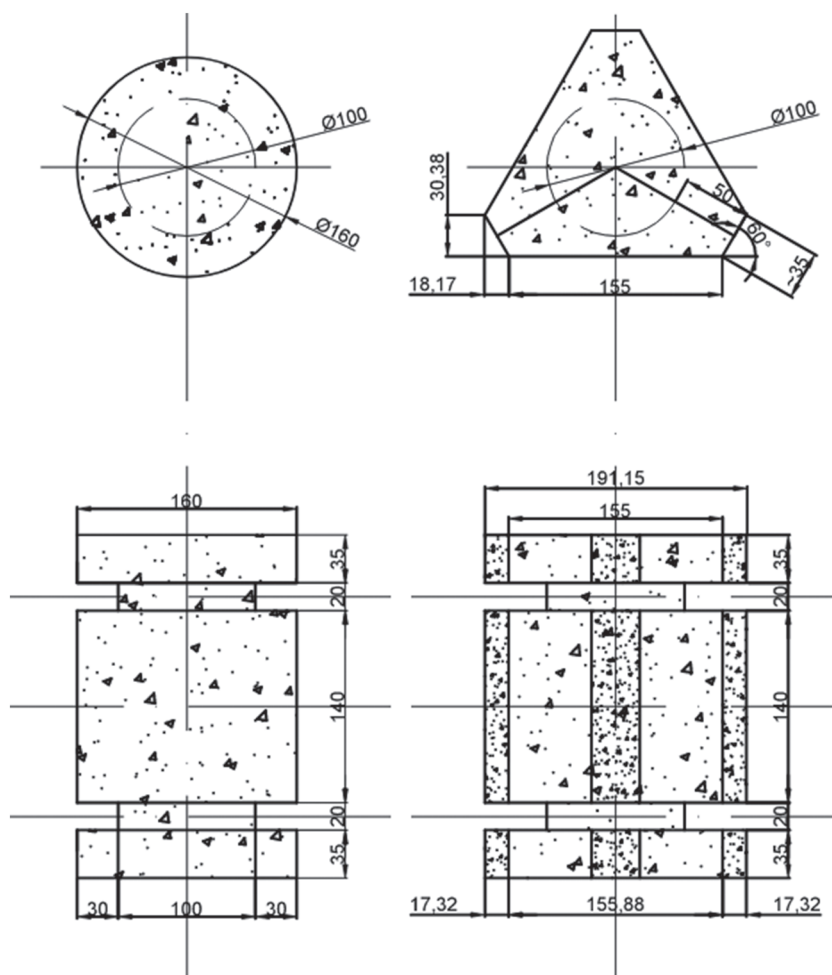


Figure 4. Block geometries used in experimental tests—cylindrical and triangular blocks, weighting 13.9 and 10.89 kg, respectively. The principal moments of inertia, for each block shape, are calculated according to the block rotation axis and are respectively 44.5 and 38.3 g·m² for cylindrical and triangular blocks. Dimensions are given in millimeters.

The camera is set up to capture 400 frames per second (fps). It is positioned on a tripod and oriented in the perpendicular direction to the plane containing the block's path (e.g., trajectory), in order to record its two-dimensional (2-D) movement during collision. The camera focuses on the area where the very first impact is supposed to occur (Figure 3). This is done to improve image resolution, in terms of pixels per unit length, and thus to increase tracked positions accuracy. A LED panel, positioned in front of the ramp, is oriented toward the impact point to limit low-light exposure zones. Extensive lighting is required due to short exposure times when acquisition frequency is high.

2.2. Concrete-Made Boulders

Concrete blocks used on collision tests are made of high-performance fiber concrete to prevent them from breaking after being repeatedly launched. Their geometry and dimensions are presented in Figure 4. They could be qualified as cylindrical shape or triangular prism with truncated vertices, but to make it simple, we will only talk in this paper about blocks having *cylindrical* or *triangular* geometries. The blocks are conceived with two parallel grooves, oriented in the perpendicular direction to the block axis, which allows them to roll or slide over the ramp. These grooves are 14 cm apart and have 2 cm wide (see Figure 4). They are designed in such a way that the blocks can, whatever their shape, move along the ramp taking support on its two lateral faces (which are 16 cm apart) with a little free margin and a minimum of friction. The blocks are thus guided on a rectilinear movement, avoiding lateral spread as much as possible. In other words, the block can roll and slide on the ramp with no lateral deviations, hitting the soil surface at the impact zone as initially planned. This block guidance allows us to obtain, as far as possible, a 2-D movement. All our analyses are based on the hypothesis of 2-D trajectories.

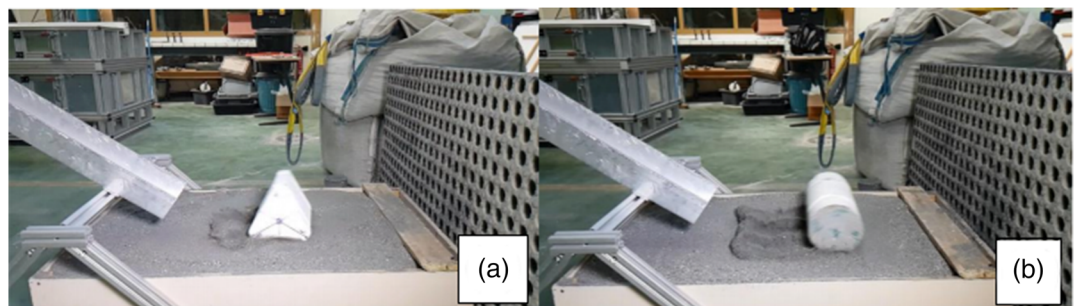


Figure 5. Screenshot of the experiments: (a) triangular block and (b) cylindrical block.

2.3. Reconstruction of Experimental Trajectories

Each one of the block launches produces a series of images where one side of the block remains visible as shown in Figure 5. The raw data resulting from image processing represents different position points on the front face of the block (one at its center, another in the edge) at regular time intervals as in Figure 6.

These data concern the block positions as the center of each block's face in both directions x and y and rotation angles measurements around the z axis (see Figure 1). Translation velocities V_{out}^x and V_{out}^y after rebound and the velocities before impact V_{in}^x and V_{in}^y are obtained from adjusting the experimental block trajectory by a second-order equation of ballistic motion. Rotational velocities ω_{out} after rebound and before impact, ω_{in} , are assumed to be constant during free flight and deduced from the rotation angle measurements before and after impact.

Figure 7 gives an illustration of the procedure for estimating block trajectories and all collision velocities. It should be noticed that the contact duration is relatively long and that the beginning and the end of the contact duration must be set up (not objectively) by the operator processing the images.

In detail, the temporal evolution of the block mass center positions (linear abscissa x and y and angular positions θ) before and after the contact period is approximated by means of polynomial regressions versus time (linear for $x(t)$ and $\theta(t)$ and second-order for $y(t)$) giving access to the velocities at any time (Figure 8). Each collision video record was submitted to this type of analysis, and the data obtained allowed statistical analysis to determine the general trends as we will see later in this work.

2.4. Sources of Errors and Uncertainties in Image Processing

The sources of errors and uncertainties are mainly due to the image processing procedure that is affected by (i) the operator subjectivity, (ii) the resulting distortions induced by camera lens, and (iii) image quality.

The operator's influence on image processing was estimated on the basis of results obtained by two separate operators following the same image processing procedure since they may affect the velocity, trajectory, and stopping distances estimation. Each operator, #1 and #2, analyzed the same data set for both cylindrical and triangular blocks and then had to perform trajectory reconstruction according to their own subjectivity. The steps consisted of the following:

- pointing, on each frame, the nearest pixels corresponding to the block's center and (for the block rotational movement) an eccentric point, both located on the visible face;
- determining the beginning and the end of the contact with the substrate; and
- determining the effective size of the pixels registered (in meters/pixels) looking to convert pixel coordinates into real coordinates and then determining the ground surface reference level.

One factor that may affect the measurement quality is the camera distance and alignment to the 2-D trajectory plane. Once the experiments were not performed at the same time and by the same operator, changing capture position may cause calibration parameters disturbance, due

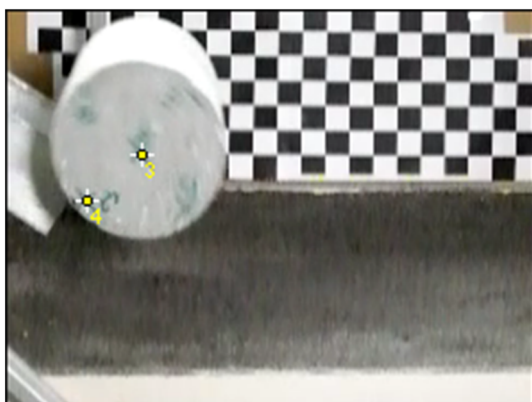


Figure 6. Pointing out an eccentric mark and the block center (video recording capture during an experimental test).

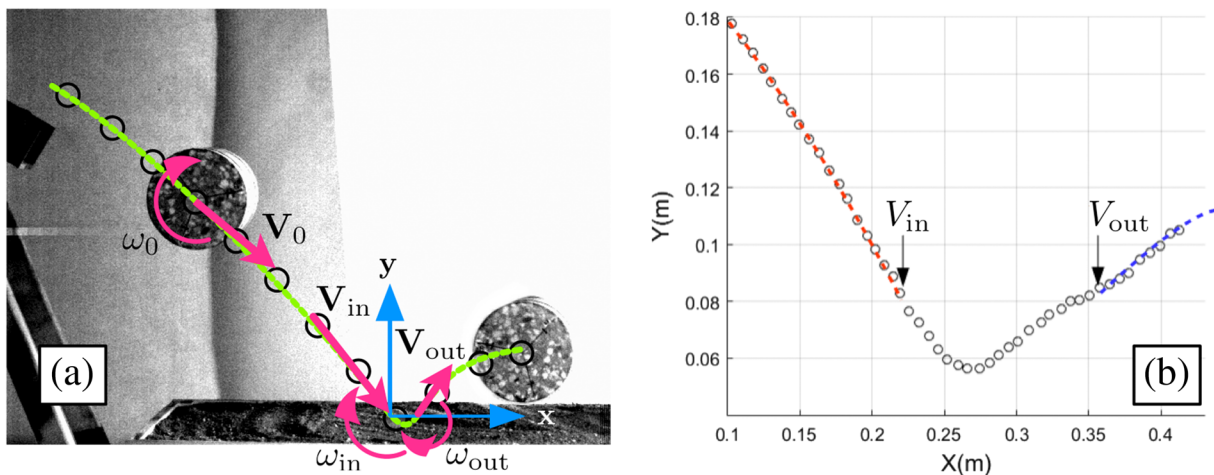


Figure 7. Block trajectory's reconstruction: (a) tracking motion and pointing procedure for incident and reflected conditions (\mathbf{V}_{in} and \mathbf{V}_{out} , respectively); and (b) identification of incident and reflected trajectories (respectively red and blue) in relation to the block center.

to new exposure and parallax conditions (perpendicularity to the view axis with respect to the trajectory's plane). This is an effect that might affect accuracy, as it is based on pointing pixels using a mouse, spreading over the effective size of pixels estimation. This last depends on their positions on a distorted image. Many authors describe it as “lens distortion” effect, for example, in the work of Zhao et al. (2014), Ahmed and Farag (2005), Heikkila et al. (1997), and Brown (1971). The method used in this study for correcting distorted images produced during a shot was the same as the one developed by Zhang (2000). The technique is based on several shots of a planar pattern from different points of view. Lens distortion equations follow nonlinear relationships between real-world coordinates (planar pattern) and camera coordinates in which components are constant and can be deduced (Brown, 1971).

Digital image quality extracted from the videos clearly influences the pointing procedure performed by different operators. Nevertheless, we observed that the variability in the distributions of incident and reflected velocities measured in the laboratory is relatively negligible compared to the different operators and the distortion caused by the optical system employed.

2.5. Experimental Results

A total of 59 experiments was performed: 28 for cylindrical blocks and 31 for triangular blocks. In order to test the influence of operator subjectivity and measurement uncertainties on the results, only the collision records of the 28 cylindrical blocks were processed independently by

1. Operator #1, *without* image distortion correction;

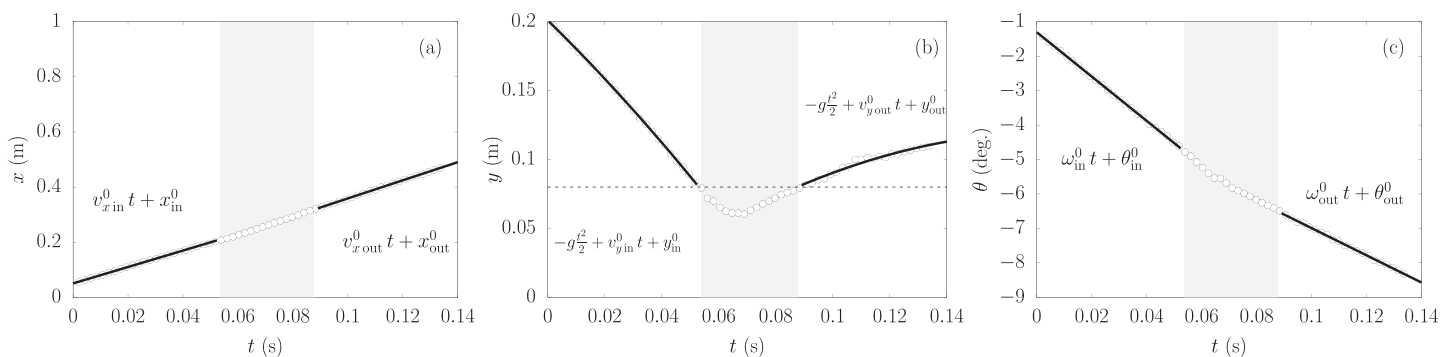


Figure 8. Block's center trajectories: shaded zones correspond to the impact duration: (a) block positions evolution before (in) and after the impact (out) over the x axis (horizontal axis) (reset to zero when block leaves the ramp); (b) vertical position evolution (over the y axis); and (c) angular position evolution in time with respect to the axis of rotation (positive z axis in the counterclockwise direction). In panel (b), dotted lines delimits a horizontal ground reference equals to 0.08 m, which corresponds to the radius of the block in the case of a cylindrical shape. The concept of contact is established on the basis of geometric considerations based on the distance between the block center and ground surface.

Table 1

Average Velocities and Standard Deviations of Two Data Sets Obtained by Both Operators (#1 and #2) Performing the Same Treatment Procedure for the Cylindrical Boulder

| | V_{in}^x m/s | V_{out}^x m/s | V_{in}^y m/s | V_{out}^y m/s | ω_{in} rad/s | ω_{out} rad/s |
|--------------------------------|--------------------------|---------------------------|--------------------------|---------------------------|-------------------------------|--------------------------------|
| Operator #1 | 3.0 ± 0.2 | 3.1 ± 0.4 | -2.4 ± 0.2 | 0.8 ± 0.2 | -63.6 ± 5.8 | -38.9 ± 6.7 |
| Operator #2 | 2.9 ± 0.2 | 3.0 ± 0.3 | -2.3 ± 0.2 | 0.9 ± 0.2 | -65.0 ± 5.8 | -42.3 ± 10.7 |
| Operator #2 (corrected images) | 2.7 ± 0.2 | 2.8 ± 0.4 | -2.2 ± 0.2 | 0.6 ± 0.2 | -64.7 ± 7.3 | -42.1 ± 10.5 |

Note. Operator #2 also performed an analysis using images whose distortion has been corrected.

2. Operator #2, *without* image distortion correction; and
3. Operator #2, with *corrected* image distortion.

For the cylinder, the average values and standard deviations of collision velocities are given in Table 1. It is interesting to note that, for travel velocities, the standard deviations are similar. However, the average values differ by a few tenths of a meter per second. For rotational velocities, the differences are in the order of a few radians per second, which seems to be a rather small variation.

Operator changes and image distortion influence are verified through cumulative distribution function (i.e., CDF) curves of collision velocities presented in Figure 9. In this paper, unlike probability density functions (PDFs), CDFs are constructed by ordering the completeness of the data. Thus, the curves are much more detailed than a PDF that would be constructed by counting for a few intervals. However, CDF curve interpretation is tricky: There is no correspondence between points with the same cumulative probability density. To be clearer, this means that an incident velocity and a reflected velocity with the same cumulative

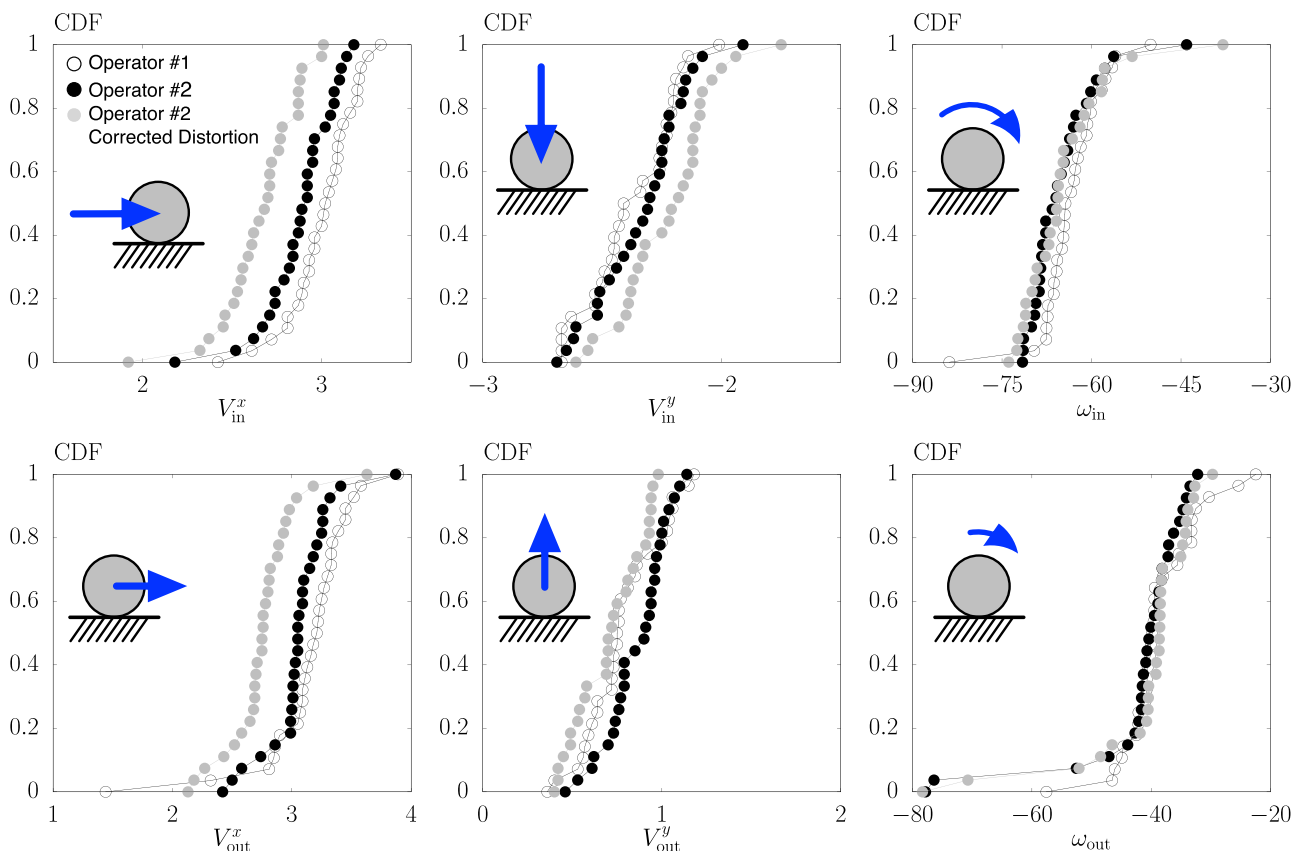


Figure 9. Cumulative distributions of incident velocities (top graphs) and reflected velocities (bottom graphs) for cylindrical specimens according to the operator and image correction. Empty circles: Operator #1, uncorrected images; solid black circles: Operator #2, uncorrected images; and solid gray circles: Operator #2, corrected images. Travel velocities are given in m/s and rotational velocities in rad/s.

Table 2
Incidental and Reflected Velocities of the 28 Cylindrical Blocks and of the 19 Triangular Blocks Retained, Obtained by Operator #2 (Uncorrected Images)

| | V_{in}^x m/s | V_{out}^x m/s | V_{in}^y m/s | V_{out}^y m/s | ω_{in} rad/s | ω_{out} rad/s |
|---------------------------|--------------------------|---------------------------|--------------------------|---------------------------|-------------------------------|--------------------------------|
| Cylindrical blocks | | | | | | |
| Average | 2.87 | 3.05 | -2.34 | 0.86 | -65.03 | -42.30 |
| Standard deviation | 0.21 | 0.28 | 0.19 | 0.17 | 5.85 | 10.68 |
| Coefficient of variation | 7% | 9% | -8% | 20% | -9% | -25% |
| Minimum | 2.18 | 2.42 | -2.69 | 0.46 | -71.57 | -77.82 |
| Maximum | 3.18 | 3.87 | -1.91 | 1.14 | -44.06 | -32.21 |
| Triangular blocks | | | | | | |
| Average | 3.76 | 2.64 | -2.73 | 0.51 | -39.70 | -17.32 |
| Standard deviation | 0.95 | 1.19 | 0.84 | 0.26 | 17.08 | 6.70 |
| Coefficient of variation | 25% | 45% | -31% | 52% | -43% | 39% |
| Minimum | 2.30 | 0.24 | -4.34 | 0.18 | -68.49 | -27.65 |
| Maximum | 5.69 | 5.87 | -1.45 | 1.19 | -13.34 | 2.41 |

probability density probably do not correspond to the same release. A second point that may help the interpretation of the CDFs is to keep in mind that the CDF refers to the complete PDF (another way of saying that densities are cumulative). Therefore, the slope inclination at a point of the CDF curve (i.e., the derivative with respect to the treated variable) is directly correlated to the PDF value at the same point. In other words, a horizontal line translates into a zero probability, while a vertical asymptotic curve would mean that the probability tends to become greater. In Figure 9, we observe that there are slight differences between the distributions obtained by the two operators but that they are quite similar on their overall appearance. CDF curves for translation velocities are invariably shifted in the same direction (i.e., increase or decrease in absolute values) depending on the operator performing image treatment or image correction. This indicates that a systematic error is introduced in the image processing procedure, which is certainly related to the determination of pixel size. This idea is strengthened by analyzing rotational velocity CDFs, which, as expected, do not seem to be affected by systematic errors. It can be seen, still in this same figure, that the uncertainties are distributed around the same mean value in a very similar way regardless of the operator, the kinematic variable measured, and whether the image is corrected or not.

Subsequently, our analysis focused on the measurements obtained by Operator #2, which was the only one among the two operators to have performed experiments for both cylinders and triangular blocks. In this way, we were able to keep some control over the effect of the subjectivity of a single individual on the results. The mean values and standard deviations of the velocities obtained are summarized in Table 2 for cylindrical and triangular blocks (28 and 19 releases, respectively). The complete results for this operator for each of the releases (cylindrical and triangular blocks) can be found in Appendix A. To complete the results of Figure 9, the curves of cumulative distributions of collision of all velocities (CDFs) for triangular shapes were established considering all performed releases (Figure 10).

3. A Kinematic Approach With Stochastic Parameters

In order to check if incident and reflected velocities can be linked to a correlation matrix composed by stochastic parameters, we have plotted on Figure 11 the cumulative distributions for cylindrical and triangular shapes, which present all the incident and reflected velocities obtained by Operator #2.

We see that, in upper graphs, corresponding to cylindrical block collisions, the incident and reflected velocity values are extremely condensed. With the exception of very few high rotational velocities, cumulative distributions of reflected velocities appear as a simple shift of the incident velocities. This reflects the good repeatability of the measurements, which testifies to the quality of both the experimental setup and image analysis.

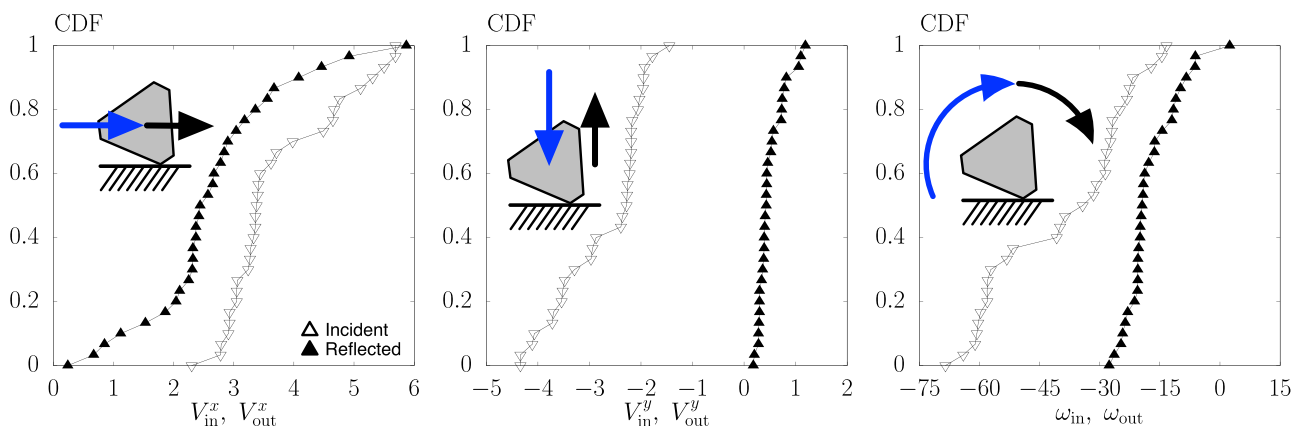


Figure 10. Cumulative distributions of incident and reflected velocities for triangular shapes according to Operator #2 (uncorrected images).

For a rebound, it is expected that the amplitude of the reflected velocities will be smaller than that of the incident velocities. This is the case for V_y and ω , but the reflected horizontal velocities are slightly higher than the incident horizontal velocities: $V_{out}^x > V_{in}^x$. This can be explained by a transformation from incident rotational velocities to horizontal velocities. There is a small loss of rotational energy that is recovered and transformed into a gain of horizontal translation energy through friction between the block and the sandy substrate. The remaining energy losses occur through the substrate by more or less complex passive soil forces and indentation mechanisms (Gracia Danies, 2018).

In view of the experimental results, a trajectory collision model in the form $\mathbf{V}_{out} = \mathbf{A} \cdot \mathbf{V}_{in}$ (Dorren et al., 2006) could be proposed. Considering a variation in velocities around an average value, it seems quite acceptable

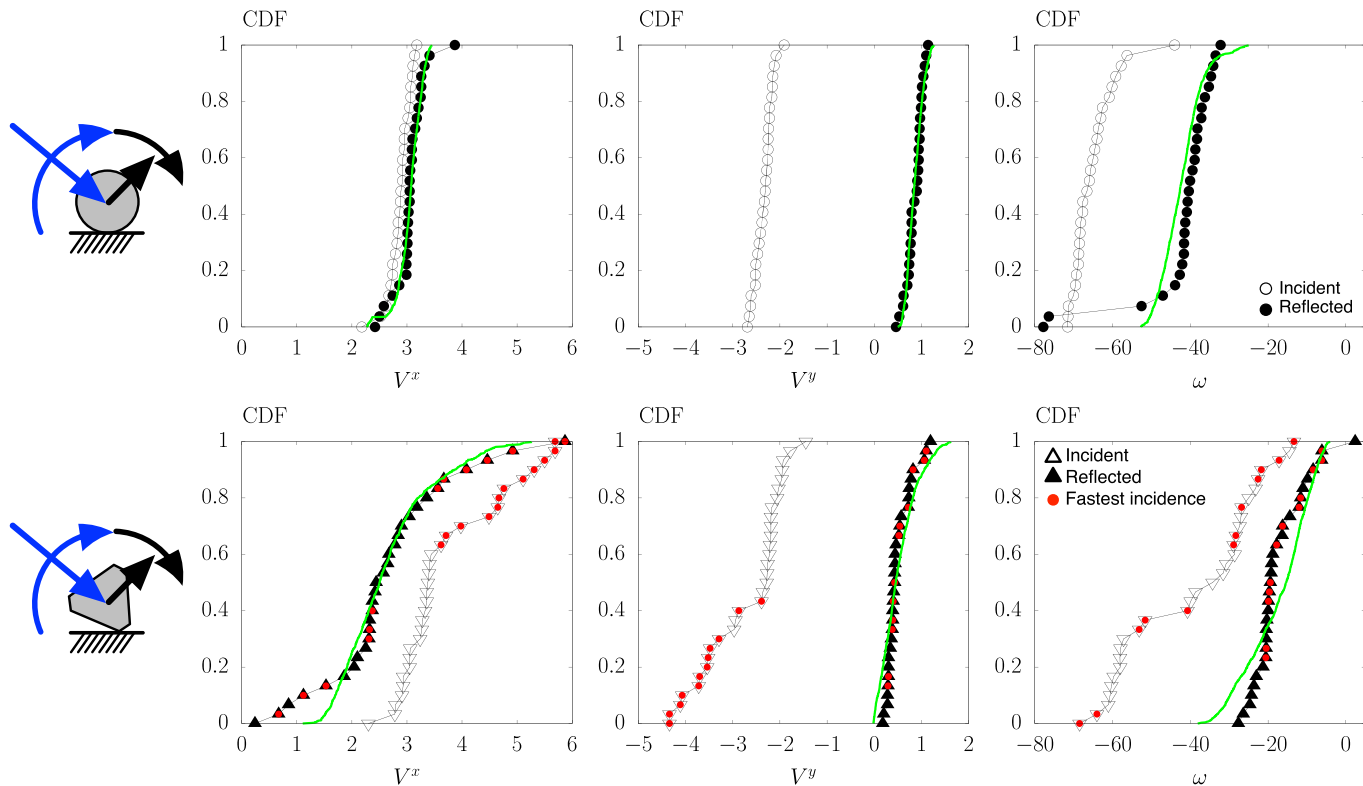


Figure 11. Cumulative distributions of rebound velocities for cylindrical and triangular shapes. Upper curves for low incident velocities and lower curves for higher incident velocities. The empty symbols correspond to the incident velocities (V_{in}^x , V_{in}^y , and ω_{in}) and the solid symbols to the reflected velocities (V_{out}^x , V_{out}^y , and ω_{out}). Green curves are those predicted by the trajectory collision model. Travel velocities are given in meters per second (m/s) and rotational velocities in radians per second (rad/s).

Table 3

Parameters of Equation 2 Obtained From the Experimental Rebounds: $A_{..} = \langle V_{out}^* \rangle / \langle V_{in}^* \rangle \pm \Delta A_{..}$

| | A_{xx} | A_{yy} | $A_{\theta\theta}$ |
|-----------------------------------|------------------|------------------|--------------------|
| Cylinders | 1.06 ± 0.027 | -0.37 ± 0.11 | 0.65 ± 0.09 |
| Triangles | 0.70 ± 0.23 | -0.19 ± 0.19 | 0.44 ± 0.15 |
| Triangles ($V_{in}^x < 3.5$ m/s) | 0.75 ± 0.22 | -0.21 ± 0.19 | 0.45 ± 0.15 |
| Triangles ($V_{in}^x > 3.5$ m/s) | 0.64 ± 0.21 | -0.16 ± 0.10 | 0.41 ± 0.04 |

Note. To use the stochastic-kinematic model, a value is extracted from uniform distributions given in the range $[A_{..} - \Delta A_{..}; A_{..} + \Delta A_{..}]$ for each single rebound.

to define the collision kinematics by linking the reflected velocities to the incident velocities considering velocity restitution coefficients defined themselves by uniform distributions and constructed as average velocity ratios (Equation 2).

$$\begin{pmatrix} V_{out}^x \\ V_{out}^y \\ \omega_{out} \end{pmatrix} = \begin{bmatrix} A_{xx} \pm \Delta A_{xx} & 0 & 0 \\ 0 & A_{yy} \pm \Delta A_{yy} & 0 \\ 0 & 0 & A_{\theta\theta} \pm \Delta A_{\theta\theta} \end{bmatrix} \cdot \begin{pmatrix} V_{in}^x \\ V_{in}^y \\ \omega_{in} \end{pmatrix} \quad (2)$$

with

$$A_{xx} = \langle V_{out}^x \rangle / \langle V_{in}^x \rangle, \quad A_{yy} = \langle V_{out}^y \rangle / \langle V_{in}^y \rangle, \quad A_{\theta\theta} = \langle \omega_{out} \rangle / \langle \omega_{in} \rangle$$

and

$$\begin{aligned} \Delta A_{xx} &= \frac{1}{4} \left| \frac{\max(V_{out}^x)}{\max(V_{in}^x)} - \frac{\min(V_{out}^x)}{\min(V_{in}^x)} \right| \\ \Delta A_{yy} &= \frac{1}{4} \left| \frac{\max(V_{out}^y)}{\max(V_{in}^y)} - \frac{\min(V_{out}^y)}{\min(V_{in}^y)} \right| \\ \Delta A_{\theta\theta} &= \frac{1}{4} \left| \frac{\max(\omega_{out})}{\max(\omega_{in})} - \frac{\min(\omega_{out})}{\min(\omega_{in})} \right| \end{aligned}$$

The assumption of a diagonal matrix implying no coupled interaction between translational and rotational reflected velocities was first tested for cylindrical shapes. The identified values of the diagonal components of the \mathbf{A} matrix deduced directly from the experimental data are given in Table 3.

Reflected velocities deduced from the trajectory collision model using these parameters are plotted in green in Figure 11. The good agreement between the green curves and the experimental results shows that this simple kinematic model proposed works rather well when applied to cylindrical blocks. It is important to notice that the parameters of Equation 2 were not adjusted but determined directly from the image analysis data. An adjustment of these parameters would rather allow a much better superposition of the curves, especially for ω_{out} values.

Observations become much less obvious when we look over triangular block's graphs (bottom graphs on Figure 11). Let's start by analyzing the appearance of the CDF of V_{in}^x (empty triangular symbols). Up to $V_{in}^x \simeq 3.5$ m/s, the curve is quite similar to what was observed for cylindrical blocks, but an inflection appears then, showing higher horizontal velocities ($V_{in}^x > 3.5$ m/s) with a lower probability density (i.e., slope). These releases correspond to the symbols identified by red dots in the CDF graphs. It is difficult to understand why there are two characteristic velocities (which would correspond to two modes or peaks in the PDF curves) with triangular blocks. Normally, the initial angular position of the block when placed at the top of the ramp should not influence its velocity at the end of the ramp, nor should the horizontal velocity in the free flight area be affected. The anomaly was then possibly originated from the launch pad or over the ramp. One possible explanation is that undesired lateral friction at the grooves induces a nonconstant moment in the direction of rotation of the block due to a fluctuating exposed surface for the triangular shape, whereas this surface is constant in the case of a cylindrical shape. Another explanation would be a slight shift in the center of rotation relative to the center of mass that would be greater for triangular shape, causing more pronounced effects.

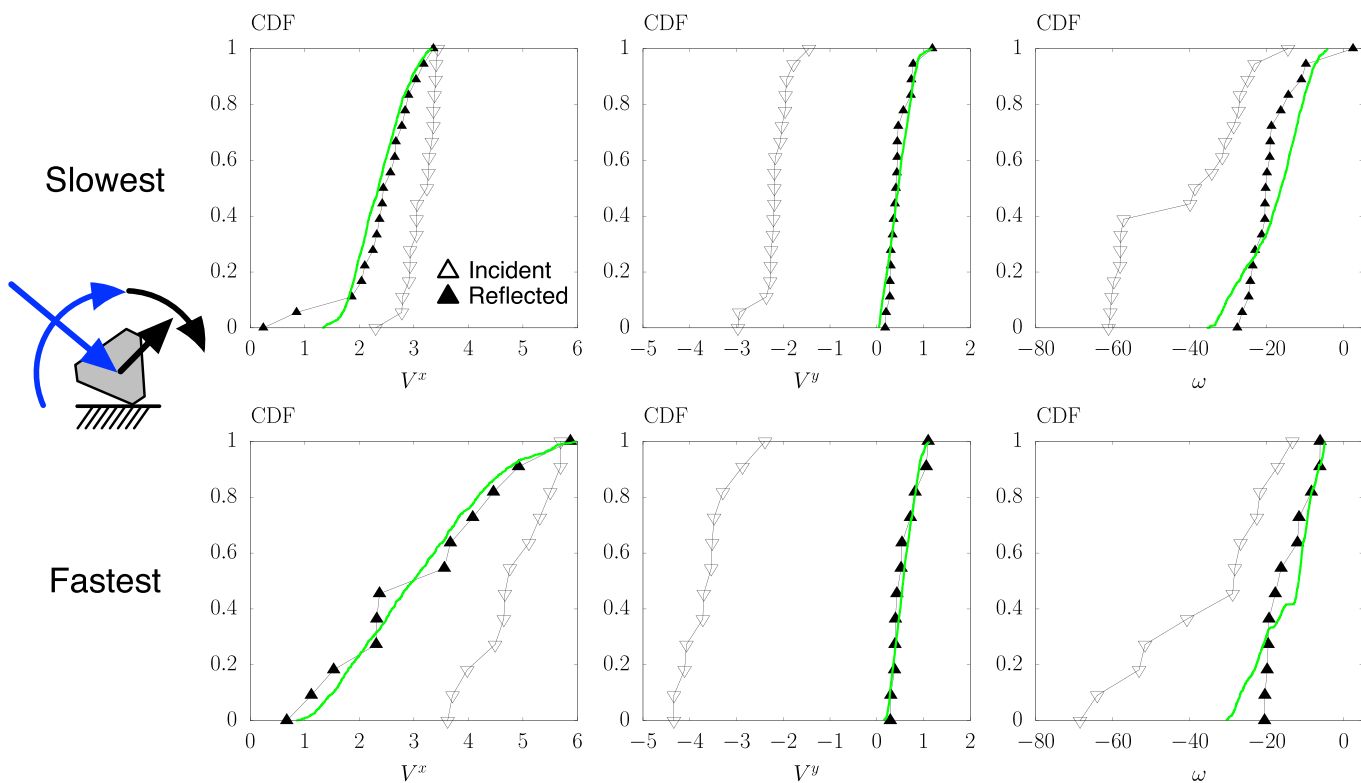


Figure 12. Cumulative distributions of collision velocities for triangular shapes, distinguished by two incident velocities: slowest incident velocities (upper graphs) and fastest incident velocities (lower graphs). Open symbols correspond to incident velocities (V_{in}^x , V_{in}^y , and ω_{in}), and solid symbols refer to reflected ones (V_{out}^x , V_{out}^y , and ω_{out}). Green curves represent reflected velocity CDFs as predicted by the stochastic model (Equation 2) by using the parameters of Table 3. The units of velocities are meters per second (m/s) for translations and radians per second (rad/s) for rotations.

We verified that there was no correlation between incident configurations and horizontal velocity for triangular blocks. This is absolutely in line with the fact that the horizontal velocity is supposed to remain constant during the free flight phase. In any case, there are indeed two typical incident configurations for triangular blocks with clearly different characteristics. It would therefore be desirable to separate the data according to their horizontal incidence rates as shown in Figure 12.

Before commenting on these new curves, it is satisfying to note that a kinematic rebound model works rather well on all the data for triangular blocks (green curves in the second line of the Figure 11). Nevertheless, this model behaves even better on each of the data sets (two types of incidence configuration) as shown in Figure 12. We can see that with this distinction, despite the impoverishment of statistical data, the reflected velocity distributions are more regular (uniform or Gaussian), which seems more in line with what is expected. It therefore appears that the CDF curves in Figure 11 for triangular blocks actually result from a combination of the distributions of the two incidence kinematic configurations. It is then interesting to note that, when returning to Figure 11, the triangular blocks that arrive with the highest horizontal velocities arrive with the highest vertical velocities; on the other hand, the rotational velocities are arbitrary.

Another observation is that kinematic restitution A_{xx} is less than 1 for triangular blocks, while it was slightly more than 1 for cylindrical blocks. This case with $A_{xx} > 1$ corresponds to the transformation of rotational into translational kinematic energy and may also result from the assumption of null out-of-diagonal terms. It can be explained by a more localized or “perforating” indentation for triangular blocks, which increases the soil’s ability to decrease block’s horizontal spreading. One would expect to observe a clear influence of the incidence angle α_{in} of the triangular blocks, but our data set does not allow us to evidence this. This may be related to the fact that the experimental setup did not allow a wide range of incident angles to be achieved.

4. 2-D-DEM Simulations Implying a Dissipative Collision Model

In the previous section, the stochastic method applied to experimental data describes the rebound phenomenon in terms of the total kinematics. Even if it works rather well, this approach does not account

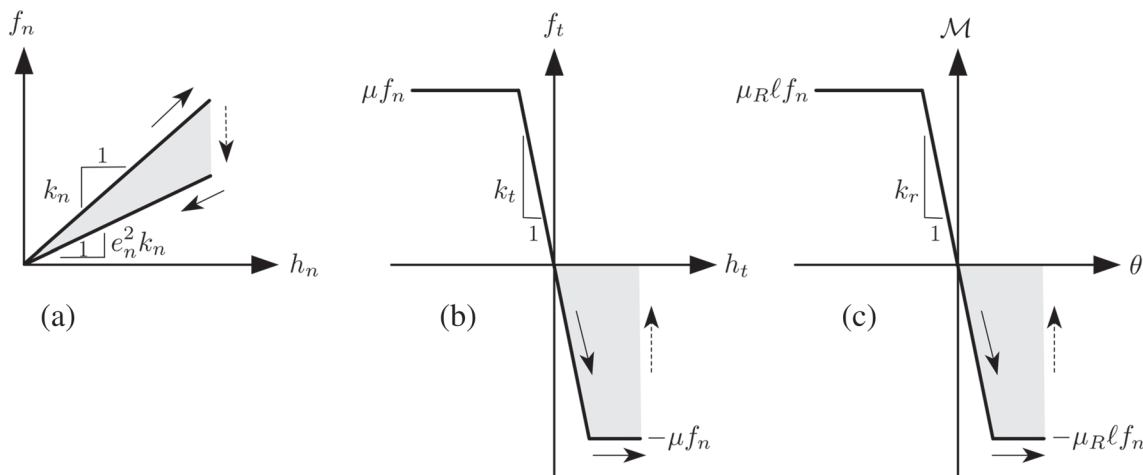


Figure 13. Illustration showing the contact laws for (a) the normal force f_n , (b) the tangent resistance force at f_n constant, and (c) the resistance moment at f_n constant. The respective stiffnesses k_n , k_t , and k_r , as well as the dissipation parameters e_n^2 , μ , and μ_R , are represented. Gray areas represent the work of the different forces until the contact is lost.

for block geometry and physical mechanisms that cause the overall energy losses. The DEM simulations performed, in a way similar to the experimentations, are 2-D collision calculations of both cylindrical and triangular blocks that impact a flat horizontal substrate (soft ground). They make it possible to explicitly take into account the shapes of the blocks and to reflect the dissipation at the point of contact. The actions to be considered at the contact points are the normal force f_n , which is perpendicular to the surface of the substrate, the tangential force f_t , and a resistant moment M . The parameters useful to account for the rebound concern elastic contact parameters (k_n , k_t , and k_r) and dissipative ones (e_n^2 , μ , and μ_R), which are presented in detail in the following section. Numerical contact parameters are determined on the basis of experimental results obtained for both triangular and cylindrical shapes. The optimization of the contact parameters was applied for the two block shapes studied in this work considering that the indentation of the soil by a wedge-shaped block implied specific modes of energy dissipation. In order to validate the DEM approach, a Monte Carlo method was applied. Finally, to define the relevance of the dissipative contact parameters on the results, a sensitivity analysis was conducted by means of a Sobol test, a method for the statistical evaluation of the sensitivity of single or coupled parameters (Sobol, 2001; Zhang et al., 2015), see Appendix B.

4.1. Dissipative Contact/Collision Model

In the framework of this study, we use simple linear elastic laws allowing a dissipation of kinematic energy in the normal, tangential, and rotational directions as described in Richefeu and Villard (2016). The associated elastic stiffnesses are, respectively, k_n , k_t , and k_r , which need to be large enough to ensure limited interpenetration and rapid mobilization of friction. The contact forces are updated at each time step by following a velocity Verlet time-explicit integration scheme (Verlet, 1967), which basically consists in injecting the estimation of the second derivative (acceleration) of position in between two half increments of its first derivative (velocity).

The normal force is updated at each explicit time increment δt with a law (Banton et al., 2009) that can be summarized as follows:

$$f_n(t + \delta t) = \begin{cases} f_n(t) - k_n \dot{h}_n(t) \delta t & \text{if } \dot{h}_n \geq 0 \text{ (loading)} \\ -k_n e_n^2 \dot{h}_n(t) \delta t & \text{if } \dot{h}_n < 0 \text{ (unloading)} \end{cases} \quad (3)$$

where e_n^2 is the energy restitution coefficient in the normal direction of contact, and \dot{h}_n is the normal relative velocity between the boulder and the substratum (which is fixed). It is important to notice that the force is calculated incrementally under load (as the bodies approach) and directly in discharge. This implies a force jump that will not affect the overall calculation in a block fall or avalanche problem. Figure 13a illustrates the evolution of the normal force f_n during a collision as a function of the penetration h_n of the bodies at a contact point. The shaded area represents the energy lost in this case, and it is easy to show that this amount of energy is $1 - e_n^2$.

Thus, energy's restitution coefficient e_n^2 can be imagined as the rebound of a mass block m falling vertically on a horizontal surface, without generating dissipation or gain of kinetic energy in the horizontal direction neither in rotation. In this situation, the energy after the collision relative to the energy before the collision is

$$\frac{\frac{1}{2}m(V_{\text{out}}^y)^2}{\frac{1}{2}m(V_{\text{in}}^y)^2} = e_n^2 \iff e_n \stackrel{\text{def}}{=} -\frac{V_{\text{out}}^y}{V_{\text{in}}^y} \quad (4)$$

This illustrates well why the restitution coefficient is denoted as the square of the kinematic restitution e_n , which is a velocity ratio (and not an energy one). Another reading of the parameter e_n^2 may be to say that it would be the ratio between the maximum height h_{out} obtained after the collision, divided by the release height h_{in} of a body. It might be useful to stress one point here concerning Equation 4 that assumes a collinear collision (i.e., velocity and contact normal vectors are collinear). Indeed, in the occurrence of a noncollinear collision, as is inherently the case in this study, the restitution measure $e_y = -V_{\text{out}}^y/V_{\text{in}}^y$ may become greater than unity. This looks like energy production but is rather related to the fact that the impacting block is considered as a whole, and it is not just related to the forces at the point of contact. This seemingly paradoxical circumstance was extensively studied by several authors who proposed alternative definitions of restitution based on impulse (e.g., Wang & Mason, 1992) or energy (e.g., Stronge, 1990) to overcome it. An instructive discussion on this particular point can be found in Lorenz et al. (1997). The particular conditions of rebounds on soft substratum of this study imply that the restitution e_y will remain lower than unity, even if it could be higher without any physical inconsistency as discussed in Louge and Adams (2002). It makes the identification $e_n = e_y$ of Equation 4 reasonably valid. To better satisfy the physical requirement for non-energy production implied by Equation 3, see Figure 13a. A more appropriate definition of the coefficient e_n would use the normal, incident, and reflected relative velocities at the point of contact; however, this point may shift during the collision.

The tangential force f_t is updated, incrementally, at each time step as follows:

$$f_t(t + \delta t) = \min (f_t(t) - k_t \dot{h}_t(t) \delta t; -\mu f_n \text{ sign}(\dot{h}_t(t))) \quad (5)$$

where \dot{h}_t is the relative sliding velocity, the function $\text{sign}(x)$ returns ± 1 depending on the sign of x , and the dissipation parameter μ includes friction and other dissipation mechanisms acting in the tangential direction (soil hardening, abutment, etc.). Each tangential force increment $k_t \dot{h}_t \delta_t$ acts in the opposite direction to the slip. The parameter μ can translate all the mechanisms involved in a collision as long as the resulting loss of kinetic energy is in the tangential direction (Richefeu, 2005; Richefeu & Villard, 2016). Figure 13b illustrates the law for tangential force in the particular situation where the normal force is constant. This situation is highly unlikely to happen during the collision, but the main purpose in this work is to simply explain how the model works. The gray area corresponds to the energy that would be dissipated if the contact were suddenly lost. We see, in this usual case for an impact, that the elastic energy is not restored. This side effect can be made imperceptible in an energy balance by using a large enough k_t stiffness value.

The resistant moment \mathcal{M} is calculated using a quite similar law to the friction law. It is called rolling friction. The purpose of the resistant moment introduced in this dissipative model is to account for the action of soft grounds (bumpy or indented), which could affect block rotation. It is calculated as follows:

$$\mathcal{M}(t + \delta t) = \min (\mathcal{M}(t) - k_r \dot{\theta}(t) \delta t; -\mu_R \ell f_n \text{ sign}(\dot{\theta}(t))) \quad (6)$$

where $\dot{\theta}$ is the relative rotational velocity, and μ_R is the coefficient of dissipation for rotation. Since μ_R is dimensionless, a length ℓ is introduced as a lever arm. This length is defined as the smallest distance between the contact point and the axis passing through the center of mass of the block and oriented as its instant rotational vector (perpendicular to the trajectory plane, which is imposed in our case). Each moment increment $k_r \dot{\theta} \delta_t$ acts in the opposite direction of the block rotation. Figure 13c illustrates resistant moment law assuming a constant normal force f_n and also a constant lever arm ℓ .

4.2. Determination of DEM Collision Parameters

DEM collision parameters distributions were determined by comparison between the experimental results and those obtained numerically using similar geometries and initial launch conditions (Figures 14a and 14b for the cylindrical and triangular blocks, respectively).

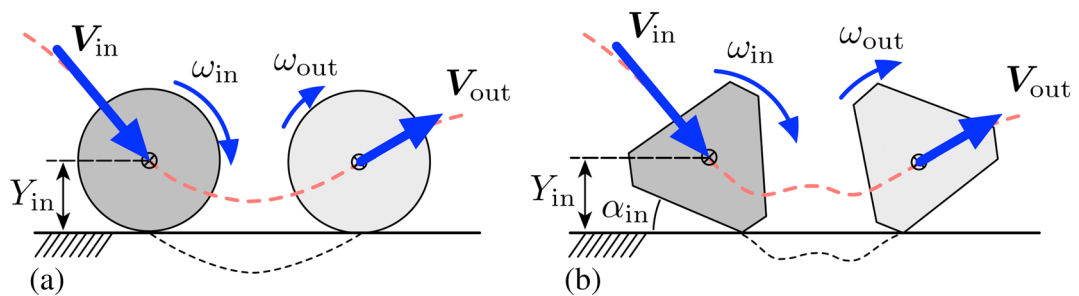


Figure 14. Initial configurations, at the beginning of each DEM simulation, identified on the experimental videos for the blocks: (a) cylindrical and (b) triangular. Initial velocities are the incident velocities ($V_0 = V_{in}$). The incident angle α_{in} corresponds to the inclination of the triangular block with respect to the horizontal plane measured on the images. The initial height Y_{in} is chosen to have a positive and almost zero ground-block deviation.

For a given set of dissipation parameters, the reflected velocities that are computed ($V_{out}^{x\text{simu}}$, $V_{out}^{y\text{simu}}$, and $\omega_{out}^{\text{simu}}$) are compared to the reflected values (V_{out}^x , V_{out}^y , and ω_{out}) obtained experimentally in order to determine the most suitable set of contact parameters that reproduces reality as its best.

To do so, a systematic procedure was implemented to optimize the parameters that control kinetic energy dissipation (e_n^2 , μ , and μ_R). This procedure is based on the minimization of an error function that estimates the squared normalized difference between computed and experimental reflected velocities:

$$Err(e_n^2, \mu, \mu_R) = \sum \left(\frac{V_{out}^{x\text{simu}} - V_{out}^x}{V_{out}^x} \right)^2 + \sum \left(\frac{V_{out}^{y\text{simu}} - V_{out}^y}{V_{out}^y} \right)^2 + \sum \left(\frac{\omega_{out}^{\text{simu}} - \omega_{out}}{\omega_{out}} \right)^2 \quad (7)$$

where reflected velocities obtained by simulation depend on e_n^2 , μ , and μ_R . We previously checked that the dependency to k_n , k_t , and k_r was observed to be very limited since they provided large enough stiffness values. It means that those values were insensitive. Hence, the numerical method chosen to perform this minimization is the Powell's conjugate direction method, which employs a finite difference scheme to define the required gradients (Press et al., 2007). Optimization starts by assuming initial values for all the parameters and modifies them all at the same time—in a multivariate way—in order to minimize the error function $Err(e_n^2, \mu, \mu_R)$.

This optimization procedure was applied to all experimental measures, for cylindrical and triangular block geometries, to highlight the difference in dissipative mechanisms involved during impact as a function of the block shapes. We were able to check for each one of the releases that

- a solution is quickly obtained even if six parameters are optimized at the same time;
- the sensitivity to the initial values is insignificant (i.e., local minimum, if they exist in the multivariate function Err , do not directly toward “wrong” solution values); and
- the stiffness parameters (k_n , k_t , and k_r) definitely do not influence the result since they are high enough. The final optimized solutions were therefore carried out by fixing the stiffness values, where $k_n = k_t = 10^7$ N/m and $k_r = 10^8$ Nm/rad.

Table 4 presents, respectively for cylindrical and triangular blocks, the optimized parameter values (mean \pm standard deviation for all the releases and for each parameter) and also for different data sets (obtained by Operators #1 and #2 as well as by image correction). We noticed a fairly strong influence of the average values depending on the operator and the image distortion correction, but the variation ranges (standard deviations) are relatively insensitive. This follows the same logic discussed previously about the kinetic restitution parameters of the matrix A .

If we compare the two sets of parameters obtained for the two shapes released, we notice that the average values obtained for e_n^2 are lower for triangular blocks than for cylindrical blocks, while the parameters μ and μ_R are higher. These differences are related to the different impact conditions between the two shapes and in particular to a greater indentation of the soil caused by the corners of triangular shapes, which leads to variable contact surfaces and soil abutment that prevent the block from moving further.

Table 4
Dissipation Parameters Obtained by Optimization for Operators #1 and #2 and for Corrected Images (Mean \pm Standard Deviation)

| | e_n^2 | μ | μ_R |
|---------------------------|-----------------|-----------------|-----------------|
| Cylindrical blocks | | | |
| Operator #1 | 0.09 ± 0.06 | 0.22 ± 0.11 | 0.24 ± 0.11 |
| Operator #2 | 0.15 ± 0.06 | 0.23 ± 0.11 | 0.16 ± 0.04 |
| Corrected images (Op. #2) | 0.12 ± 0.06 | 0.33 ± 0.20 | 0.20 ± 0.16 |
| Triangular blocks | | | |
| Operator #1 | 0.05 ± 0.08 | 0.38 ± 0.18 | 0.32 ± 0.18 |
| Operator #2 | 0.03 ± 0.03 | 0.48 ± 0.21 | 0.39 ± 0.22 |

4.3. Validation of the Identified Dissipation Parameters

The objective of this section is to show that the DEM model described previously, when coupled with a Monte Carlo method, allows the experimental results (translation and rotational velocities from a known statistical distribution of input values) to be correctly reproduced when considering cylindrical shapes. Monte Carlo simulations are based on a sample selected from a generation of random values contained in known statistical distributions (Raychaudhuri, 2008). In this way, this sampling represents the input variables of a function that are randomly selected from a range of known values. The incident velocities are taken as the average values obtained by Operator #2 for cylinders so that the initial high with respect to the ground is equal to the radius of the cylinder, and the initial velocities are $V_x^0 = \langle V_{\text{in}}^x \rangle = 2.9 \text{ m/s}$, $V_y^0 = \langle V_{\text{in}}^y \rangle = -2.3 \text{ m/s}$, and $\omega^0 = \langle \omega_{\text{in}} \rangle = -65 \text{ rad/s}$. The output data are the reflected velocities $\mathbf{V}_{\text{out}} = (V_{\text{out}}^x, V_{\text{out}}^y, \omega_{\text{out}})$, which can be characterized by their statistical distribution curve (here represented by CDFs). It becomes thus possible to compare the distributions issued from Monte Carlo realizations involving DEM simulations with those obtained experimentally instead of comparing a single condition.

First, the simplest distribution assumption for the input variables was made in order to reduce the accuracy of the data measured by image analysis and to avoid any bias. Uniform distributions of input values were therefore used:

$$\text{CDF}(x | a, b) = \int_a^x \frac{1}{b-a} dx = \frac{x-a}{b-a}, \text{ where } a \leq x < b \quad (8)$$

where a is the minimum value and b the maximum value that the real parameter x can have. Of course, it must be ensured that the variation range of a parameter is compatible with its physical meaning ($e_n^2 \in [0.0, 1.0]$, $\mu > 0$ and $\mu_R > 0$). The following analysis was based on the mechanical parameters (e_n^2 , μ , and μ_R) identified by Operator #2 for cylindrical blocks. The distributions of these parameters are presented in Figure 15 and compared to the retained uniform distributions which are characterized by $e_n^2 \in [0.05, 0.25]$, $\mu \in [0.0, 0.6]$, and $\mu_R \in [0.0, 0.3]$. Once the distributions of the input parameters have been established, the Monte Carlo method can be applied. A total of 50,000 simulations were performed. Figure 16 shows the distributions of the reflected velocities (V_{out}^x , V_{out}^y , and ω_{out}) resulting from this method, compared to the values actually obtained by Operator #2 by image processing. The good agreement between experimental and

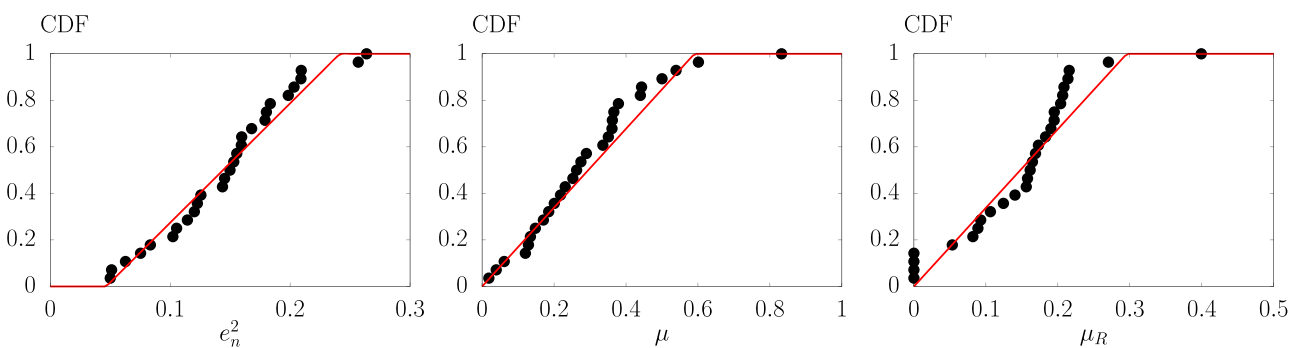


Figure 15. Cumulative frequency distributions of the parameters identified by Operator #2 (optimization) compared to the uniform distributions selected.

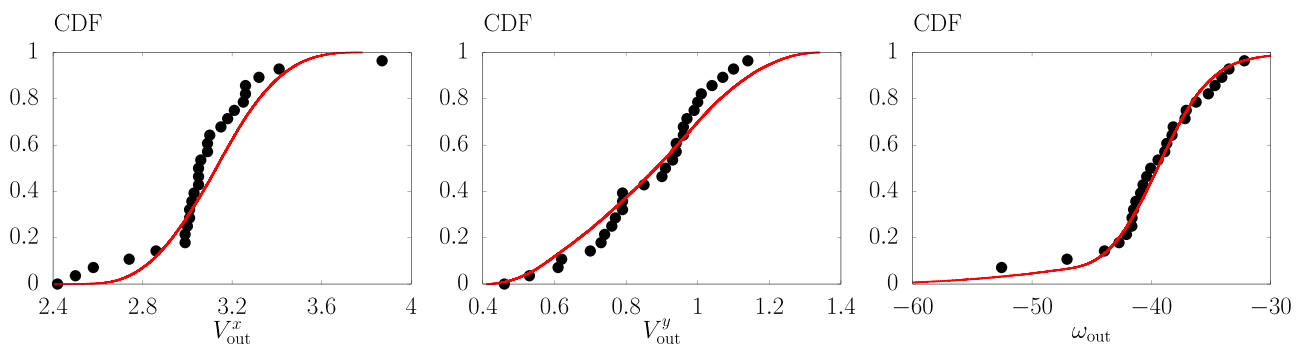


Figure 16. Cumulative frequency distributions of reflected velocities for cylindrical blocks determined by Operator #2 and predicted by the discrete model.

predicted cumulative frequency distribution shows that the numerical process used to calibrate the numerical contact parameters is relevant and that the DEM model is able to reproduce the rebound variability accounting for relatively simple distribution of parameters. In particular, it is interesting to note the extreme similarity of the curves for rotational velocities. This numerical approach, based on the definition of simple parameter distributions, can be extended to real observations obtained in the field when only a few amount of rebounds can be identified.

4.4. Sensitivity Analysis

With the objective of studying the responsiveness of DEM predictions as a function of the dissipation parameters, a sensitivity analysis was conducted by means of Sobol tests (Sobol, 2001; Zhan et al., 2013). This method is often used to identify the parameters that most affect the response of numerical simulations. In this study, the Sobol tests are performed with a Monte Carlo strategy called “one factor at a time” (OFAT) (Iooss & Lemaître, 2015; Zhan et al., 2013). It consists in varying a single input variable at a time in order to determine the variance of output measures in response, with the other input parameters being set at their average values. Only the weight of the variation of the analyzed variable is extracted from the output responses (in this case, the velocities reflected in the three directions). More than 50,000 collision simulations involving cylindrical blocks were performed for the three input variables, which are the DEM dissipation parameters: e_n^2 , μ , and μ_R . Since these parameters have been identified in a previous section, their values are drawn randomly within their distributions (see Figure 15).

Figure 17a shows the first-order sensitivity indices S_i , with $i = e_n^2, \mu$, or μ_R , for the output variables V_{out}^x , V_{out}^y , and ω_{out} . Similarly, the second-order sensitivity indices (S_{ij}) are presented in Figure 17b for the pairs of input variables (i, j): $(e_n^2 - \mu)$, $(\mu - \mu_R)$, and $(\mu_R - e_n^2)$. For details on how these indices are computed, see Appendix B.

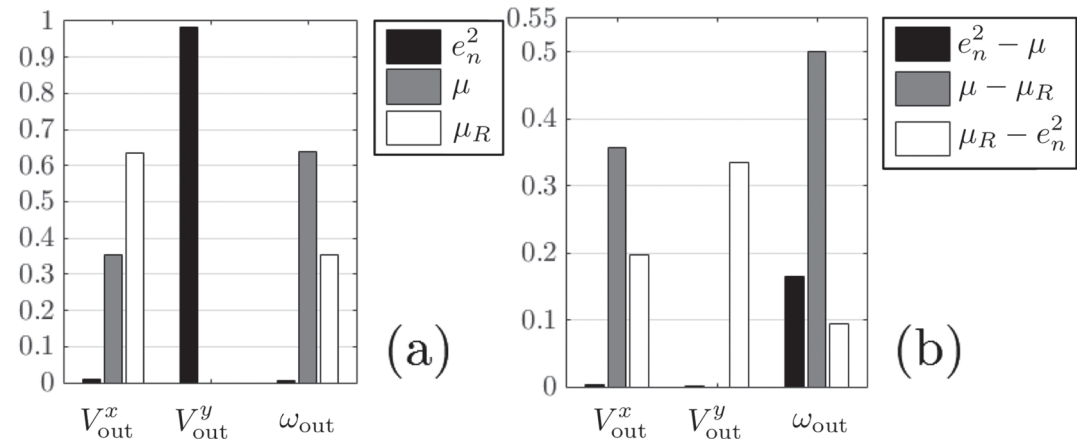


Figure 17. (a) First-order Sobol index and (b) second-order Sobol index for the cylindrical boulder.

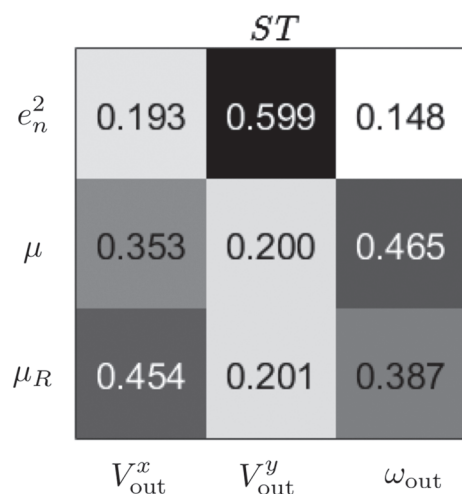


Figure 18. Total Sobol sensitivity index (ST). A 3×3 matrix displaying the contribution values of each dissipation parameter on each output data.

The role played, at the first order, by e_n^2 on the reflected vertical velocity is exclusive. It is thus possible to compare the value of A_{yy}^2 , obtained for the stochastic model, with the value of e_n^2 , considering that these two ratios represent the square of the ratio between reflected and incident velocities. Considering the analysis carried out with the results of Operator #2, we have obtained a value of $A_{yy}^2 = (0.37 \pm 0.11)^2 \simeq 0.149 \pm 0.08$ (Table 3), which is very close to the value of $e_n^2 = 0.15 \pm 0.06$ (Table 4, Operator #2) that validates the two numerical solutions for the assessment of these parameters. The variables μ and μ_R influence both the velocities V_{out}^x and ω_{out} in a coupled manner. It is important to note that the variable μ has a more significant effect than the variable μ_R on the reflected rotational velocities ω_{out} . Surprisingly, this propensity is reversed for reflected horizontal velocities V_{out}^x , which seems to be more sensitive to μ_R . That said, this distribution of influence weights between μ and μ_R may be related to the input kinematic configuration and is important to highlight the joint action of these two dissipation parameters on horizontal and rotational reflected velocities. As a consequence, direct comparison between these coefficients, that have a real physical meaning, with the coefficients of the stochastic matrix A_{xx} and $A_{\theta\theta}$ cannot be made. Second-order Sobol

indices are more difficult to interpret. Let us simply remember that these indices, in addition to transcribing a simultaneous role of two input variables, focus on the unexplained variance at the first order. As an example, for the vertical reflected velocity, the few cases that are not explainable by e_n^2 could be explained by the joint action of e_n^2 and μ_R . The strong interaction obtained between all the dissipative parameters on the reflected rotational velocity demonstrates that the mechanism involved in rotation is very complex (*i.e.*, difficult to predict).

Figure 18 shows the calculated values of the total Sobol sensitivity indices (ST), which estimate the contribution of the i variable to the different output variances, including any variance caused by its interactions with other input variables and of any order. This means that we can sort the isolated effects of the coupled contributions and obtain the relevant contributions of each parameter on the reflected velocities.

The data shown in Figure 18 confirm what was observed from the first- and second-order indices. To be very synthetic, let's say that e_n^2 alone controls the reflected vertical velocity, while the other reflected velocities can be adjusted by both parameters μ and μ_R almost independently of e_n^2 . The practical side of this observation is the determination of dissipation parameters for real cases. This result confirms also that a slight change in the μ_R significantly affects the reflected velocities in the horizontal direction (V_{out}^x). This means that for the fixed values of e_n^2 and μ in a simulation, if we only change the value of μ_R , V_{out}^x undergoes a large change, which shows that it is extremely sensitive to changes in μ_R . The same relationship can be established for μ in the reflected rotational velocity ω_{out} . It is important to recall that these results are only valid for the range of input velocities derived from the experimental tests described in section 2.5.

5. Conclusions

In this work, we aimed to analyze the effect of block shape on the rebound parameters variability using experimental data and numerical simulations. The experimental campaign consisted in releasing blocks of cylindrical and triangular shapes under controlled conditions in laboratory and identifying, from a kinematic analysis and a mechanical-probabilistic coupling, the restitution coefficients and DEM rebound parameters (e_n^2 , μ , and μ_R) that better reproduce the experimental observations.

From the experiments, it was concluded that the trajectory variability for triangular blocks is much wider than for cylindrical ones. Due to the regularity of the cylindrical shape, they always impact the substrate with a similar configuration (*i.e.*, smooth surface). On the other hand, triangular blocks can impact the ground on a side or a corner. Therefore, the shape of the block plays a major role in ground indentation, which points out its relevance in energy dissipation mechanisms.

It was shown that it is possible to establish a simple kinematic rebound model that can be applied to the experimental data. The results of this analysis show that the proposed stochastic model presents a good agreement with the experimental observations, both for cylindrical and triangular blocks. This model is represented by a linear relationship between incident and reflected velocities, where the contact parameters

can be randomly and uniformly selected between two limits. In the context of the trajectory analysis, the latter parameters could be adjusted from experimental tests or impact simulations, thus leading to abacuses conception, depending on soil type and block shape.

An optimization procedure was tested to determine the rebound parameters in DEM that better reproduce the experimental results for blocks of cylindrical or triangular shapes. Given the different impact conditions between the two types of block (greater indentation of the ground by the triangular shapes, which leads to stop mechanisms that oppose block movement), two distinct sets of parameters have been established. With regard to the characterization of these parameters, the restitution coefficients e_n^2 in the normal direction are lower for triangles, while the parameters μ and μ_R are higher. Upon parameter determination, comparisons between experimental and numerical results were made to demonstrate the predictive capability of the numerical model (Monte Carlo simulations for the cylindrical shape). Although some disparities were observed in this analysis, which reflect the uncertainties that were mainly related to the processing of experimental data, the results obtained are very satisfactory.

Finally, a sensitivity analysis was performed to assess the impact of a perturbation applied to the input variables on the output results from a given set of assumptions. A Sobol sensitivity analysis was used, and the main conclusions lead to that the dissipative parameters μ and μ_R appear to have a coupled effect on translation and rotational reflected velocities (V_{out}^x and ω_{out} , respectively); on the other hand, e_n^2 is the parameter that influences alone the reflected normal velocity V_{out}^y .

Even if these analyses are developed on small-scale experiments, the approach proposed in this paper can be applied to any experimental data (if the recordings are available and the procedure can be applied following the overall proceedings detailed in the first section) or simulated with any numerical models. One can expect that a systematic analysis of a large data set of collisions involving various conditions (such as different substrates, shapes, slopes, and ranges of incident velocities) would lead to a functional database that could be used by engineers in the future.

Appendix A: Experimental Raw Data

Raw data is provided for triangular and cylindrical blocks, in Tables A1 and A2 respectively. The incident and reflected velocities, identified by image processing, are given by separating the translation and rotation components.

Table A1
Incident and Reflected Velocities for 31 Launches of Triangular Blocks

| V_{in}^x (m/s) | V_{out}^x (m/s) | V_{in}^y (m/s) | V_{out}^y (m/s) | ω_{in} (rad/s) | ω_{out} (rad/s) |
|----------------------------|-----------------------------|----------------------------|-----------------------------|---------------------------------|----------------------------------|
| 4.67 | 1.53 | -3.70 | 0.54 | -21.73 | -8.40 |
| 4.49 | 5.87 | -4.34 | 1.10 | -64.03 | -19.66 |
| 2.79 | 2.32 | -1.96 | 0.74 | -23.20 | -19.94 |
| 3.36 | 0.85 | -2.97 | 0.46 | -27.32 | -11.02 |
| 4.76 | 2.37 | -3.52 | 0.39 | -22.58 | -6.15 |
| 3.41 | 2.04 | -2.94 | 0.20 | -25.00 | -9.84 |
| 5.11 | 4.46 | -3.54 | 0.72 | -68.49 | -17.80 |
| 5.69 | 4.92 | -4.07 | 0.82 | -53.17 | -19.42 |
| 3.98 | 2.31 | -2.87 | 0.38 | -17.17 | -12.01 |
| 5.50 | 3.56 | -4.11 | 0.29 | -28.87 | -19.89 |
| 5.69 | 3.67 | -3.48 | 0.43 | -28.30 | -20.57 |
| 3.71 | 0.67 | -3.29 | 0.52 | -13.34 | -6.21 |
| 4.65 | 1.12 | -4.34 | 1.06 | -26.83 | -16.28 |
| 5.31 | 4.08 | -3.72 | 0.30 | -51.62 | -20.49 |
| 3.44 | 2.25 | -2.03 | 0.28 | -28.59 | -18.79 |
| 3.40 | 2.10 | -2.06 | 0.43 | -26.96 | -24.28 |
| 2.93 | 2.84 | -1.78 | 0.44 | -38.65 | -20.46 |
| 2.30 | 0.24 | -1.95 | 0.18 | -14.50 | 2.41 |

Table A1 (continued)

| V_{in}^x (m/s) | V_{out}^x (m/s) | V_{in}^y (m/s) | V_{out}^y (m/s) | ω_{in} (rad/s) | ω_{out} (rad/s) |
|----------------------------|-----------------------------|----------------------------|-----------------------------|---------------------------------|----------------------------------|
| 3.28 | 2.57 | -2.19 | 0.30 | -57.97 | -27.65 |
| 3.06 | 3.36 | -1.93 | 0.73 | -60.32 | -16.37 |
| 3.36 | 2.44 | -1.45 | 0.39 | -31.55 | -24.69 |
| 3.05 | 3.18 | -2.22 | 0.41 | -58.05 | -20.30 |
| 2.78 | 2.67 | -2.28 | 0.36 | -60.65 | -20.49 |
| 3.62 | 2.32 | -2.39 | 0.40 | -40.73 | -11.62 |
| 3.38 | 2.65 | -2.17 | 0.57 | -30.79 | -23.65 |
| 2.91 | 2.37 | -2.21 | 0.28 | -39.90 | -19.21 |
| 3.24 | 1.86 | -2.27 | 0.30 | -34.27 | -14.40 |
| 3.33 | 2.90 | -2.26 | 0.78 | -57.18 | -21.31 |
| 2.93 | 2.78 | -2.19 | 0.44 | -61.10 | -26.38 |
| 3.27 | 2.42 | -2.19 | 0.34 | -58.11 | -23.02 |
| 3.05 | 3.04 | -2.36 | 1.19 | -59.72 | -19.12 |

Table A2
Incident and Reflected Velocities for 28 Launches (Cylindrical Blocks)

| V_{in}^x (m/s) | V_{out}^x (m/s) | V_{in}^y (m/s) | V_{out}^y (m/s) | ω_{in} (rad/s) | ω_{out} (rad/s) |
|----------------------------|-----------------------------|----------------------------|-----------------------------|---------------------------------|----------------------------------|
| 2.52 | 3.32 | -2.65 | 0.90 | -68.77 | -40.90 |
| 3.02 | 3.01 | -1.91 | 0.77 | -67.68 | -38.88 |
| 2.92 | 3.41 | -2.38 | 1.00 | -65.71 | -34.67 |
| 2.84 | 3.09 | -2.36 | 0.91 | -64.58 | -32.21 |
| 2.84 | 3.02 | -2.33 | 0.61 | -71.46 | -37.18 |
| 2.87 | 3.06 | -2.16 | 0.85 | -71.40 | -40.70 |
| 2.88 | 2.42 | -2.62 | 0.73 | -69.32 | -47.07 |
| 2.18 | 3.87 | -2.25 | 0.74 | -44.06 | -43.93 |
| 3.07 | 3.26 | -2.52 | 0.94 | -67.68 | -38.17 |
| 2.95 | 3.03 | -2.47 | 0.96 | -68.20 | -40.39 |
| 2.62 | 2.74 | -2.28 | 0.79 | -63.68 | -35.23 |
| 2.95 | 2.58 | -2.24 | 0.46 | -68.52 | -76.40 |
| 3.07 | 2.50 | -2.52 | 0.53 | -64.00 | -34.10 |
| 3.05 | 3.15 | -2.31 | 0.79 | -71.57 | -41.30 |
| 2.74 | 2.86 | -2.26 | 0.70 | -70.07 | -52.55 |
| 2.74 | 3.05 | -2.44 | 0.96 | -65.08 | -39.44 |
| 2.96 | 3.25 | -2.51 | 1.14 | -65.96 | -41.64 |
| 3.14 | 3.18 | -2.69 | 1.01 | -69.53 | -41.62 |
| 3.18 | 3.21 | -2.41 | 0.76 | -60.86 | -33.50 |
| 2.92 | 2.99 | -2.08 | 0.79 | -57.78 | -37.08 |
| 2.79 | 2.99 | -2.15 | 1.10 | -68.70 | -40.06 |
| 2.71 | 3.10 | -2.22 | 0.93 | -56.28 | -42.09 |
| 2.82 | 3.05 | -2.30 | 1.04 | -62.62 | -42.71 |
| 2.89 | 3.05 | -2.25 | 0.99 | -59.18 | -77.82 |
| 2.67 | 3.00 | -2.61 | 0.62 | -68.36 | -38.27 |
| 3.11 | 3.09 | -2.12 | 1.07 | -63.02 | -36.25 |
| 2.92 | 3.01 | -2.17 | 0.97 | -60.14 | -41.49 |
| 3.10 | 3.26 | -2.22 | 0.94 | -66.60 | -38.71 |

Appendix B: Sobol Analysis

The total variance of reflected velocities can be calculated through the following expression:

$$\text{Var}(\mathbf{V}_{\text{out}}) = \sum_{i=1}^n V_i + \sum_{i \leq j \leq n} V_{ij} + \dots + \sum_{i \leq n} V_{1\dots n} \quad (\text{B1})$$

where $\mathbf{V}_{\text{out}} = \{V_{\text{out}}^x, V_{\text{out}}^y, \omega_{\text{out}}\}$ corresponds to the output vector and V_i expresses the first-order effect of each input parameter Y_i (e_n^2 , μ or μ_R) on the output vector. The other Y terms are higher-order effects obtained by varying several input parameters at the same time.

The first-order sensitivity index S_i , where i is one of the input parameters, is calculated using the following expression:

$$S_i = \frac{V_i}{\text{Var}(\mathbf{V}_{\text{out}})} \text{ where } V_i = \text{Var}[\mathbb{E}(\mathbf{V}_{\text{out}}|Y_i)] \quad (\text{B2})$$

This index can be interpreted as the variance share of an output parameter (a reflected velocity) explained by the variation of the input parameter i (dissipation DEM parameter) independently of the value of the other factors.

The second-order sensitivity index S_{ij} is defined by

$$S_{ij} = \frac{V_{ij}}{\text{Var}(\mathbf{V}_{\text{out}})} \text{ where } V_{ij} = \text{Var}[\mathbb{E}(\mathbf{V}_{\text{out}}|Y_i, Y_j)] - V_i - V_j \quad (\text{B3})$$

This is the part of the variance of an output parameter due to changes in two input parameters i and j that is not explained by the sum of their own effects.

The total sensitivity index ST_i is calculated as follows:

$$ST_i = 1 - \frac{\text{Var}(\mathbb{E}(\mathbf{V}_{\text{out}}|Y_{\sim i}))}{\text{Var}(\mathbf{V}_{\text{out}})} \quad (\text{B4})$$

where $\sim i$ corresponds to the contribution of all parameters, except to the parameter i .

Data Availability Statement

The figure data set is stored in figshare (<https://doi.org/10.6084/m9.figshare.11522088>).

Acknowledgments

The authors thank G. Vian for the conception and construction of this experimental device. Z. Ftouni and F. Asadi are also warmly thanked for their support in carrying out the experimental release tests. This study was funded by the French company IMSRN (<https://www.groupegincer.com/filiales/imsrn/>). The Laboratoire 3SR is part of the Idex Cross Disciplinary Project RISK “Managing risk for a more resilient world” (<https://risk.univ-grenoble-alpes.fr>).

References

- Ahmed, M., & Farag, A. (2005). Nonmetric calibration of camera lens distortion: Differential methods and robust estimation. *Transactions on Image Processing*, 14(8), 1215–1230. <https://doi.org/10.1109/TIP.2005.846025>
- Asteriou, P., & Tsiambaos, G. (2016). Empirical model for predicting rockfall trajectory direction. *Rock Mechanics and Rock Engineering*, 49(3), 927–941.
- Banton, J., Villard, P., Jongmans, D., & Scavia, C. (2009). Two-dimensional discrete element models of debris avalanches: Parameterization and the reproducibility of experimental results. *Journal of Geophysical Research*, 114, F04013. <https://doi.org/10.1029/2008JF001161>
- Bourrier, F., Berger, F., Tardif, P., Dorren, L., & Hungr, O. (2012). Rockfall rebound: Comparison of detailed field experiments and alternative modelling approaches. *Earth Surface Processes and Landforms*, 37(6), 656–665. <https://doi.org/10.1002/esp.3202>
- Bourrier, F., Dorren, L., Nicot, F., Berger, F., & Darve, F. (2009). Toward objective rockfall trajectory simulation using a stochastic impact model. *Geomorphology*, 110(3), 68–79. <https://doi.org/10.1016/j.geomorph.2009.03.017>
- Bourrier, F., & Hungr, O. (2011). *Rockfall dynamics: A critical review of collision and rebound models*: Wiley Online Library.
- Bourrier, F., Nicot, F., & Darve, F. (2008). Physical processes within a 2D granular layer during an impact. *Granular Matter*, 10(6), 415–437. <https://doi.org/10.1007/s10035-008-0108-0>
- Brown, D. (1971). Close-range camera calibration. *Photogrammetric Engineering*, 37(8), 855–866.
- Chau, K. T., Wong, R. H. C., & Wu, J. J. (2002). Coefficient of restitution and rotational motions of rockfall impacts. *International Journal of Rock Mechanics and Mining Sciences*, 39, 69–77.
- Cundall, P. A., & Strack, O. D. L. (1979). A discrete numerical model for granular assemblies. *Geotechnique*, 29, 47–65.
- Dorren, L. (2016). Rockyfor3d (v5.2) revealed—Transparent description of the complete 3D rockfall model. *ecorisQ*
- Dorren, L., Berger, F., & Putters, U. S. (2006). Real-size experiments and 3-D simulation of rockfall on forested and non-forested slopes. *Natural Hazards and Earth System Sciences*, 6(1), 145–153. <https://doi.org/10.5194/nhess-6-145-2006>
- Dorren, L., & Seijmonsbergen, A. (2003). Comparison of three GIS-based models for predicting rockfall runout zones at a regional scale. *Geomorphology*, 56(1), 49–64. [https://doi.org/10.1016/S0169-555X\(03\)00045-X](https://doi.org/10.1016/S0169-555X(03)00045-X)
- Garcia, B., Villard, P., Richefeu, V., & Daudon, D. (2017). Experimental and DEM analysis of the dissipation involved in the collision of a boulder with a substratum. *EPJ Web of Conferences*, 140, 16010. <https://doi.org/10.1051/epjconf/201714016010>

- Gracia Danies, F. (2018). Application de la méthode des points matériels aux phénomènes gravitaires (Ph.D. Thesis). Univ. Grenoble-Alpes.
- Heikkila, J., Silven, O., et al. (1997). A four-step camera calibration procedure with implicit image correction. In *CVPR*, 97 (p. 1106).
- Hungr, O., & Evans, S. (1988). Engineering evaluation of fragmental rockfall hazards. In *Proceedings of the 5th Int. Symposium on Landslides, Lausanne* (pp. 685–690).
- Iooss, B., & Lemaître, P. (2015). A review on global sensitivity analysis methods. In Meloni, C., & Dellino, G. (Eds.), *Uncertainty management in simulation-optimization of complex systems: Algorithms and applications* (pp. 101–122). Springer.
- Labroue, V., & Heidenreich, B. (2009). Half-scale experimental study of rockfall impacts on sandy slopes. *Natural Hazards and Earth System Sciences*, 9(6), 1981–1993. <https://doi.org/10.5194/nhess-9-1981-2009>
- Lorenz, A., Tuozzolo, C., & Louge, M. Y. (1997). Measurements of impact properties of small, nearly spherical particles. *Experimental Mechanics*, 37(3), 292–298.
- Louge, M. Y., & Adams, M. E. (2002). Anomalous behavior of normal kinematic restitution in the oblique impacts of a hard sphere on an elastoplastic plate. *Physical Review E*, 65, 021303. <https://doi.org/10.1103/PhysRevE.65.021303>
- Manzella, I., & Labroue, V. (2008). Qualitative analysis of rock avalanches propagation by means of physical modelling of non-constrained gravel flows. *Rock Mechanics and Rock Engineering*, 41(1), 133–151. <https://doi.org/10.1007/s00603-007-0134-y>
- Manzella, I., Lisjak, A., Mahabadi, O., & Grasselli, G. (2011). Influence of initial block packing on rock avalanche flow and emplacement mechanisms through FEM/DEM simulations. In *2011 Panam-cgs Geotechnical Conference*.
- Mollon, G., Richefeu, V., Villard, P., & Daudon, D. (2012). Numerical simulation of rock avalanches: Influence of a local dissipative contact model on the collective behavior of granular flows. *Journal of Geophysical Research*, 117, F02036. <https://doi.org/10.1029/2011JF002202>
- Okura, Y., Kitahara, H., Sammori, T., & Kawanami, A. (2000). The effects of rockfall volume on runout distance. *Engineering Geology*, 58(2), 109–124. [https://doi.org/10.1016/S0013-7952\(00\)00049-1](https://doi.org/10.1016/S0013-7952(00)00049-1)
- Piteau, D., & Clayton, R. (1977). Discussion of paper computerized design of rock slopes using inter-active graphics for the input and output of geometrical data by P. Cundall. In *Proceedings of the 16th Symposium on Rock Mechanics, Minneapolis* (pp. 62–63).
- Press, W., Teukolsky, S., Vetterling, W., & Flannery, B. (2007). *Numerical recipes 3rd edition: The art of scientific computing* (3rd ed.). New York, NY, USA: Cambridge University Press.
- Raychaudhuri, S. (2008). Introduction to Monte Carlo simulation. In *Proceedings of the 40th Conference on Winter Simulation* (pp. 91–100). Winter Simulation Conference.
- Richefeu, V. (2005). Approach by 3D discrete elements of the behavior of cohesive granular materials weakly stressed (Theses, Université Montpellier II - Sciences et Techniques du Languedoc).
- Richefeu, V., & Villard, P. (2016). *Modeling gravity hazards from rockfalls to landslides*. ISTE Press Ltd, Elsevier Ltd, UK.
- Sobol, I. M. (2001). Global sensitivity indexes for nonlinear mathematical models and their Monte Carlo estimates. *Mathematics and Computers in Simulation*, 55, 271–280.
- Stronge, W. J. (1990). Rigid body collisions with friction. *Proceedings of the Royal Society of London. Series A*, 431, 169–181.
- Verlet, L. (1967). Computer “experiments” on classical fluids. I. Thermodynamical properties of Lennard-Jones molecules. *Physical Review*, 159, 98–103. <https://doi.org/10.1103/PhysRev.159.98>
- Wang, Y., & Mason, M. T. (1992). Two-dimensional rigid-body collisions with friction. *Journal of Applied Mechanics*, 59, 635–642.
- Wu, S. (1985). Rockfall evaluation by computer simulation. *Transportation Research Record*, 1031, 1–5.
- Zhan, C., Song, X., Xia, J., & Tong, C. (2013). An efficient integrated approach for global sensitivity analysis of hydrological model parameters. *Environmental Modelling and Software*, 41, 39–52. <https://doi.org/10.1016/j.envsoft.2012.10.009>
- Zhang, Z. (2000). A flexible new technique for camera calibration. *IEEE Transactions on Pattern Analysis and Machine Intelligence*, 22(11), 1330–1334. <https://doi.org/10.1109/34.888718>
- Zhang, X., Trame, M. N., Lesco, L. J., & Schmidt, S. (2015). Sobol sensitivity analysis: A tool to guide the development and evaluation of systems pharmacology models. *CPT: Pharmacometrics & Systems Pharmacology*, 4, 69–79. <https://doi.org/10.1002/psp4.6>
- Zhao, P., Zhao, W. Z., & Duan, Z. Y. (2014). A calibration method for high precision vision measurement system. In *Vehicle, mechatronics and information technologies II* (Vol. 543, pp. 1005–1008). Trans Tech Publications.